IJMMM International Journal of Minerals, Metallurgy and Materials 矿物冶金与材料学报（英文版）

Exploring the optoelectronic properties of calcium vanadate semiconductors: A combined experimental and DFT study

Xin Jin, Xianyong Ding, Guishang Pei, Shuaiqi Li, Xing'an Dong, Xiaolong Yang, Rui Wang, Peng Yu, and Xuewei Lü

Cite this article as:
Xin Jin, Xianyong Ding, Guishang Pei, Shuaiqi Li, Xing'an Dong, Xiaolong Yang, Rui Wang, Peng Yu, and Xuewei Lü, Exploring the optoelectronic properties of calcium vanadate semiconductors: A combined experimental and DFT study, *Int. J. Miner. Metall. Mater.*, 32(2025), No. 6, pp. 1417-1426. https://doi.org/10.1007/s12613-025-3095-9

INTERNATIONAL JOURNAL OF
Minerals, Metallurgy and Materials

Volume 32, Number 6, June 2025
Page 1417

Research Article https://doi.org/10.1007/s12613-025-3095-9

Exploring the optoelectronic properties of calcium vanadate semiconductors: A combined experimental and DFT study

Xin Jin[1)], *Xianyong Ding*[1,2,3)], *Guishang Pei*[4)], *Shuaiqi Li*[1)], *Xing'an Dong*[1)], *Xiaolong Yang*[5)], *Rui Wang*[5)], *Peng Yu*[1)], *and Xuewei Lü*[2,3)]✉

1) College of Physics and Electronic Engineering, Chongqing Normal University, Chongqing 401331, China
2) College of Materials Science and Engineering, Chongqing University, Chongqing 400044, China
3) Chongqing Key Laboratory of Vanadium-Titanium Metallurgy and Advanced Materials, Chongqing University, Chongqing 400044, China
4) Department of Materials Science and Engineering, Gwanak-gu, Seoul 08826, Korea
5) College of Physics & Chongqing Key Laboratory for Strongly Coupled Physics, Chongqing University, Chongqing 400044, China
(Received: 29 September 2024; revised: 14 January 2025; accepted: 14 January 2025)

Abstract: Metal vanadates garner significant interest because of their exceptional potential for use in diverse practical applications, which stems from their unique framework structures, bond strength heterogeneities, and strong O^{2-}–V^{5+} charge-transfer bands. However, their optoelectronic properties have not yet been sufficiently explored. In this study, we synthesized three high-purity calcium vanadate compounds (CaV_2O_6, $Ca_2V_2O_7$, and $Ca_3V_2O_8$) and comprehensively investigated their optoelectronic properties via first-principles calculations and experimental characterizations. CaV_2O_6, $Ca_2V_2O_7$, and $Ca_3V_2O_8$ are indirect band gap semiconductors with band gaps of 2.5–3.4 eV. A comparative analysis between density functional theory (DFT) and DFT + *U* (local Coulomb interaction, *U*) calculations revealed that standard DFT was sufficient to accurately describe the lattice parameters and band gaps of these vanadates. Further luminescence studies revealed significant photo- and electro-luminescence properties within the visible light spectrum. Notably, the luminescence intensity of CaV_2O_6 exhibited a remarkable 10-fold enhancement under a modest pressure of only 0.88 GPa, underscoring its exceptional potential for use in pressure-tunable optical applications. These findings provide deeper insight into the electronic structures and optical behaviors of vanadates and highlight their potential as strong candidates for application in phosphor materials and optoelectronic devices.

Keywords: calcium vanadate; electronic structure; optical property; high-pressure luminescence; first-principles calculations

1. Introduction

As industrialization accelerates, the global demands for sustainable energy and technology based on green materials are increasing [1–5]. Vanadium-based compounds, which are known for their diverse valence states and rich crystal structures, have become focal points in developing novel materials because of their wide ranges of potential applications [6–7]. These versatile oxidation states and complex structures render vanadium highly valuable for use in optical, electronic, and catalytic materials, with promise for application in fields such as light-emitting diodes, energy storage systems, superconductivity, and industrial catalysts. Additionally, the mechanical stabilities and high-temperature resistances of vanadium-based materials render them essential components in extreme environments and aerospace applications. These characteristics highlight the considerable importance and research potential of vanadium in modern technologies. China possesses abundant vanadium resources and places a high priority on their comprehensive development and utilization, accelerating the research and development of vanadium-based products, which is crucial in enhancing the efficient use of these resources [8–9].

Among vanadium-based materials, vanadate compounds, which are inorganic compounds containing vanadate ions, are particularly representative [10–13]. Vanadium, which is a transition metal with multiple oxidation states, forms covalent bonds with the oxygen atoms within the structures of vanadates, resulting in the formation of vanadyl polyhedra. These polyhedra can be combined in various manners via corner- or edge-sharing to form 1D, 2D, or 3D structures. The diversity and structural complexities of vanadates endow them with excellent physicochemical properties, indicating their significant potential for use in numerous applications, e.g., batteries [14–18], catalysts [19–20], optical devices [21–22], sensors [23–24], and thermoelectric materials [25–26]. Therefore, vanadate materials should be critical in advancing sustainable energy technologies and developing advanced materials.

Among the various vanadate materials, calcium vanadates (CaV_2O_6, $Ca_2V_2O_7$, $Ca_3V_2O_8$, and $Ca_4V_2O_9$) [27–28] represent a significant subclass of metal vanadates characterized by

✉ Corresponding author: Xuewei Lü E-mail: lvxuewei@163.com

their unique layered structures [29–32]. These materials exhibit remarkable chemical stabilities and photoluminescence (PL) and microwave dielectric properties. Recently, the distinct structural features of calcium vanadates attracted considerable research interest, positioning them as promising candidates for application in lithium-ion batteries (LIBs) [33], sodium-ion batteries [34], and phosphorescent materials [35]. For instance, Zhang and Wu [36] reported that $Ca_2V_2O_7$ microspheres exhibited high coulombic efficiencies, good cycling performances, and significant reversible capacities, positioning them as candidate electrode materials for use in LIBs. Additionally, Thiagarajan *et al.* [37] used chemical precipitation to synthesize a $Ca_2V_2O_7$/polyaniline composite electrode that displayed outstanding electrochemical properties, with a specific capacitance of 542 $F \cdot g^{-1}$ at a current density of 1 $A \cdot g^{-1}$. Yu *et al.* [38] synthesized CaV_2O_6 nanorods, and the presence of induced oxygen vacancies and coexisting V^{4+}/V^{5+} ions led to unusual PL and photocatalytic activities. Kaur and Khanna [39] produced $Ca_2V_2O_7$ using solid-state synthesis, and its PL spectrum showed a broad range from 350 to 600 nm, with a peak at 510 nm. Parab and Salker [40] utilized citric acid-assisted sol–gel methods to synthesize two unique sets of green $Ca_3V_2O_8$ phosphors by adjusting their luminescence ranges and efficiencies via Tb doping and Na–Tb codoping.

To fully harness the potential of calcium vanadates in existing fields and expand their application in energy and functional materials, conducting comprehensive systematic theoretical and experimental investigations of their optoelectronic properties is essential. Such research aids in understanding the fundamental principles governing the behaviors of the electronic structures of materials at the microscopic level, providing crucial theoretical support for fundamental physics. Additionally, such research has significant implications for the application of these substances as optoelectronic materials in fields such as photocatalysis and phosphor technologies.

Motivated by these factors, we systematically investigated the crystal structures, electronic properties, and luminescence characteristics of alkaline-earth-metal calcium vanadates, i.e., CaV_2O_6, $Ca_2V_2O_7$, and $Ca_3V_2O_8$, using first-principles calculations combined with experimental techniques. High-purity samples of the three vanadate compounds were synthesized and characterized via Raman and energy-dispersive spectroscopy (EDS) and X-ray diffraction (XRD). Theoretical calculations indicated that density functional theory (DFT) accurately captured the lattice parameters and band gaps. Furthermore, the three vanadates exhibited pronounced levels of PL and electroluminescence within the visible light region. Notably, the application of pressure significantly enhanced the PL intensity of CaV_2O_6, demonstrating its tunable luminescence properties. These findings enhance our understanding of the electronic structures and optical properties of calcium vanadates, rendering them promising candidates for application in photocatalysis, phosphor materials, and optoelectronic devices.

2. Experimental and calculation methods

2.1. Reactants

V_2O_5 (99.95%) and CaO (99.99%) were obtained from Shanghai Macklin Biochemical Technology (Shanghai, China) and used as received without further purification.

2.2. Preparation of CaV_2O_6, $Ca_2V_2O_7$ and $Ca_3V_2O_8$

The CaV_2O_6, $Ca_2V_2O_7$, and $Ca_3V_2O_8$ powders were prepared via straightforward solid-state reactions conducted under ambient conditions using CaO and V_2O_5 as reactants. The powders were obtained via roasting and milling at V_2O_5 : CaO molar ratios of 1:1, 1:2, and 1:3. The samples were roasted at 600°C for 20 h and then cooled in a furnace. Subsequently, the samples were crushed into pellets using a vibrating mill and calcined. Roasting and milling were repeated to yield high-purity CaV_2O_6, $Ca_2V_2O_7$, and $Ca_3V_2O_8$.

2.3. Characterization of CaV_2O_6, $Ca_2V_2O_7$ and $Ca_3V_2O_8$

CaV_2O_6, $Ca_2V_2O_7$, and $Ca_3V_2O_8$ were characterized using various analytical techniques. Scanning electron microscopy (SEM, SU-70, Hitachi, Tokyo, Japan) was used to examine the microstructures, and EDS (X-Max detector, Oxford Instruments, Abingdon, UK) was used in elemental composition analysis. The crystal structures were determined via XRD (D/Max-2400, Rigaku, Tokyo, Japan) with Cu K_α radiation (λ = 1.5406 Å), operating in a θ–2θ configuration. Ultraviolet–visible (UV–vis) diffuse reflectance spectroscopy (U-3900, Hitachi) was used to evaluate the light absorption properties. The luminescence characteristics were studied using PL spectroscopy with a 325 nm laser, whereas Raman spectroscopy (LabRAM HR, Horiba, Kyoto, Japan), with a 532 nm laser, was used to investigate the lattice vibrations. *In situ* steady-state high-pressure PL spectra were measured using a microspectroscopy system (Gora-UVN-FL, Ideaoptics, Shanghai, China) integrated with 405 and 532 nm excitation lasers. Cathodoluminescence (CL) spectroscopy of the samples was conducted using a system operating at 40 mA and 5 kV.

2.4. Computational details

The electronic energies of calcium metavanadate were investigated using the Vienna Ab initio Simulation Package (VASP, University of Vienna, Vienna, Austria) within the framework of DFT [41–42]. The generalized gradient approximation was used for the exchange-correlation functional, employing the Perdew–Burke–Ernzerhof (PBE) functional [43–44]. Additionally, the PBE solid (PBEsol) functional [43] was used to accurately optimize the lattice constants and enhance the energy calculations. The projector augmented-wave method was applied to treat the valence states of Ca ($3s^2$, $3p^6$, $4s^2$), V ($3p^6$, $3d^4$, $4s^1$), and O ($2s^2$, $2p^4$). To precisely capture the electronic band structures, the PBE + U (local Coulomb interaction, U) method was employed, with the effective correlation parameter (U_{eff}) for vanadium set in the range 0–4 eV. A plane-wave cutoff energy of 520 eV was ad-

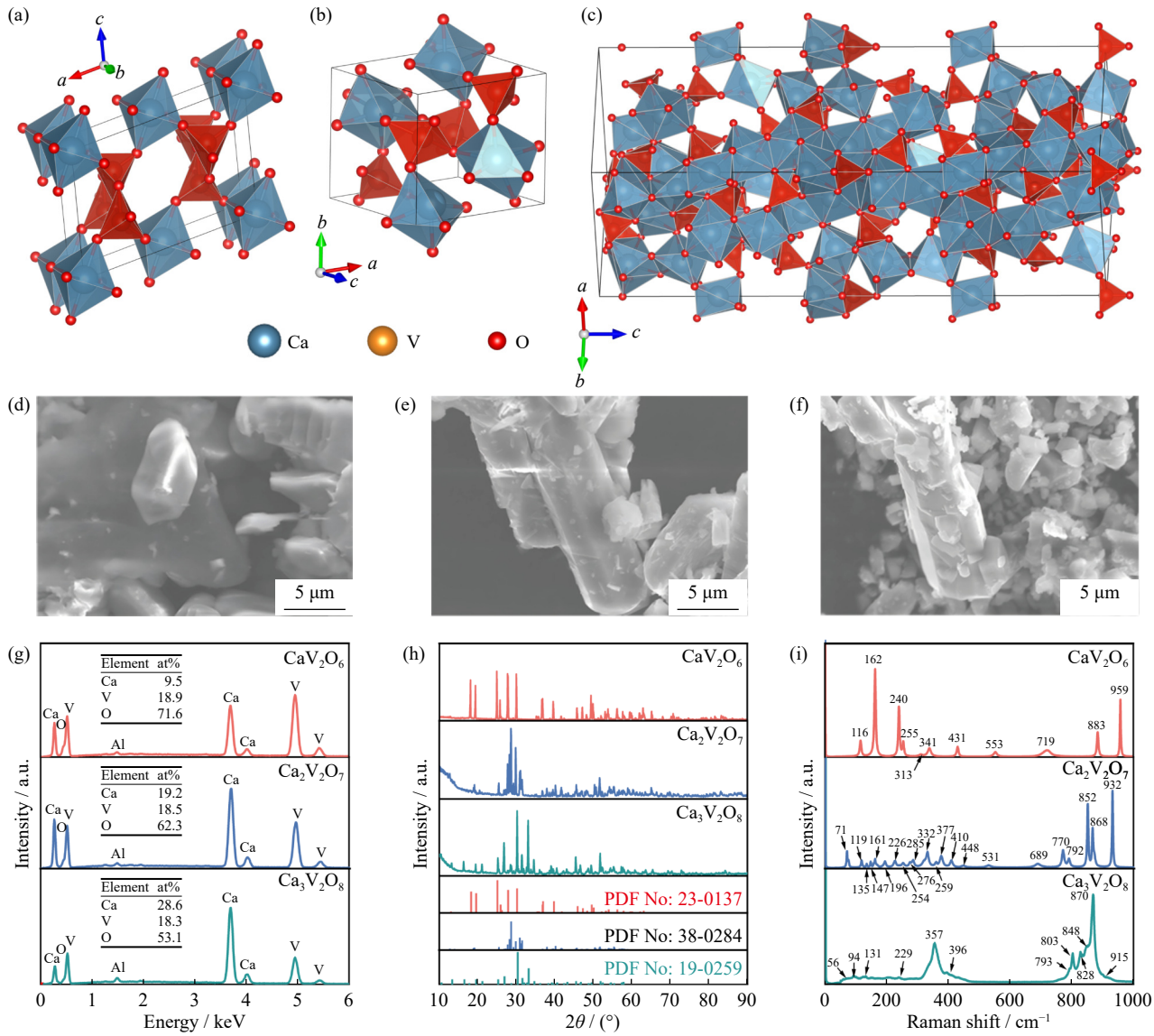

Fig. 1. Crystal structures of (a) CaV_2O_6, (b) $Ca_2V_2O_7$, and (c) $Ca_3V_2O_8$ and the coordination environments of V and Ca. SEM images of (d) CaV_2O_6, (e) $Ca_2V_2O_7$, and (f) $Ca_3V_2O_8$. Results of (g) EDS, (h) XRD, and (i) Raman spectroscopy of the as-prepared samples.

opted during crystal structure optimization and the self-consistent energy calculations. To ensure computational accuracy, the energy convergence criterion was established at 10^{-8} eV, whereas the convergence threshold for interatomic forces was set at 10^{-3} eV·Å^{-1}. Brillouin zone sampling was implemented using the Monkhorst–Pack scheme [45] with *k*-point meshes of 10 × 10 × 5, 6 × 6 × 5, and 7 × 7 × 5 for CaV_2O_6, $Ca_2V_2O_7$, and $Ca_3V_2O_8$, respectively.

3. Results and discussion

Fig. 1(a)–(c) shows the crystal structures of CaV_2O_6, $Ca_2V_2O_7$, and $Ca_3V_2O_8$. Of these, CaV_2O_6 crystallizes in a monoclinic system comprising Ca^{2+}, V^{5+}, and O^{2-} ions in the space group *C*2/*m*. In this structure, Ca^{2+} is coordinated to six O^{2-} ions, forming edge-sharing CaO_6 octahedra with Ca–O bond lengths of 2.33 and 2.36 Å. V^{5+} is bonded to five O^{2-} ions in a five-coordinate geometry, exhibiting V–O bond lengths of 1.64–1.99 Å. $Ca_2V_2O_7$ crystallizes in a triclinic system (space group *P*1), and Ca^{2+} occupies two inequivalent sites, forming distorted CaO_6 and CaO_7 geometries with six or seven O^{2-} ions, respectively, where the Ca–O bond lengths are 2.32–2.51 Å. V^{5+} is observed at two inequivalent sites, coordinating with four O^{2-} ions to form VO_4 tetrahedra, with V–O bond lengths of 1.67–2.00 Å, and the structure features seven inequivalent O^{2-} sites with diverse geometries. Finally, $Ca_3V_2O_8$ crystallizes in the trigonal system, i.e., in the space group *R*3. In this structure, Ca^{2+} occupies nine inequivalent sites, coordinating with six or seven O^{2-} ions to form CaO_6 octahedra and distorted CaO_7 geometries, while the overall structure contains 20 inequivalent O^{2-} sites. In summary, calcium vanadates exhibit unique framework structures comprising distorted VO_x and CaO_x polyhedra sharing common oxygen vertices. The complexities of their structures and heterogeneities of their bonds render calcium vanadates susceptible to intriguing physical phenomena, particularly in terms

of their electronic structures and optoelectronic properties.

Fig. 1(d)–(f) shows the SEM images of the synthesized compounds. The prepared samples comprise micron-sized particles with varying sizes, exhibiting particle size distributions of approximately 1–20 μm. The results of subsequent EDS (Fig. 1(g)) indicate that the three compounds comprise Ca, V, and O, and the corresponding molar ratios of CaV_2O_6, $Ca_2V_2O_7$, and $Ca_3V_2O_8$ are approximately 1:2:6, 2:2:7, and 3:2:8, respectively. Therefore, the structures of the three compounds are free from elemental contamination, and the presence of Al is attributed to the sample stage used during analysis.

XRD was conducted to further verify the crystalline phases of the synthesized samples. As shown in Fig. 1(h), the XRD patterns treated via Rietveld refinement indicate that the observed diffraction peaks correspond well to the standard peaks of monoclinic CaV_2O_6 (PDF #23-0137) [46], triclinic $Ca_2V_2O_7$ (#38-0284) [47], and trigonal $Ca_3V_2O_8$ (#19-0259) [48]. These results validate the crystalline structures of the target materials. Fig. 1(i) shows the Raman spectra, revealing the internal and external vibrations, in addition to the translational motions associated with the oxygen polyhedra. In the spectra of structures comprising Ca–O and V–O polyhedra, the modes observed at <400 cm^{-1} reflect polyhedral torsion and Ca^{2+} translational vibrations. By contrast, the intermediate frequency peaks (400–750 cm^{-1}) are attributed to the bending vibrations of V–O–V bridges, and the strong peaks at 750–1000 cm^{-1} are assigned to V–O bond stretching within the VO_x polyhedra [31,49–50]. These spectral features provide crucial insight into the vibrational dynamics of metavanadates. The presented experimental characterization evidence confirms that we successfully synthesized three calcium vanadates with high purities and without elemental impurities.

The structures of CaV_2O_6, $Ca_2V_2O_7$, and $Ca_3V_2O_8$ were optimized using first-principles calculations, as detailed in Table 1. The lattice parameters obtained using the PBEsol method show more reasonable deviations from the experimental measurements than those obtained using the PBE method, and the enhanced accuracy underscores the suitability of the PBEsol approach. Consequently, we utilized the PBEsol method to compute the electronic structures, thus ensuring the levels of reliability and robustness of the results. This comprehensive optimization serves as a critical foundation for further investigations of the optoelectronic properties of these calcium vanadates.

Table 1. Calculated equilibrium lattice parameters (*a*, *b*, *c*, *β*) and cell volumes of CaV_2O_6, $Ca_2V_2O_7$, and $Ca_3V_2O_8$ compared to the results of previous experimental studies

Structure	Ref./method	*a* / Å	*b* / Å	*c* / Å	*β* / (°)	Volume / Å^3
CaV_2O_6	[46]	10.060	3.675	7.040	104.843	251.597
	PBE	10.752	3.663	7.276	101.223	281.074
	Error	6.88%	0.35%	3.36%	3.45%	11.72%
	PBEsol	10.216	3.623	7.160	103.058	258.152
	Error	1.551%	−1.415%	1.705%	−1.703%	2.605%
$Ca_2V_2O_7$	[47]	6.667	6.921	7.018	63.840	288.800
	PBE	6.749	7.034	7.123	63.790	300.958
	Error	1.23%	1.633%	1.501%	−0.053%	4.210%
	PBEsol	6.645	6.926	7.007	63.874	286.996
	Error	−0.33%	0.072%	−0.157%	0.053%	−0.625%
$Ca_3V_2O_8$	[48]	10.809	10.809	38.028	90.000	3847.700
	PBE	10.737	10.737	37.875	90.000	3781.481
	Error	−0.666%	−0.666%	−0.402%	0%	−1.721%
	PBEsol	10.761	10.761	37.766	90.000	3787.111
	Error	−0.444%	−0.444%	−0.689%	0%	−1.575%

Fig. 2(a)–(c) shows the energy–volume relationships of CaV_2O_6, $Ca_2V_2O_7$, and $Ca_3V_2O_8$ obtained via DFT calculations. The data are fitted using the Birch equation in Eulerian form [51], expressed in terms of the fitting parameters *B* and *C*:

$$E(V) = E_0 + BV_0\left\{\left[\left(\frac{V_0}{V}\right)^{\frac{2}{3}} - 1\right]^2 + \frac{C}{2}\left[\left(\frac{V_0}{V}\right)^{\frac{2}{3}} - 1\right]^3\right\},$$

where $E(V)$ and E_0 respectively represent the total energy as a function of the volume (V) and minimum energy corresponding to the equilibrium volume V_0. Additionally, the bulk modulus $B_0 = 8B/9$ and $B_1 = C + 4$ respectively represent the resistance of the material to compression and pressure derivative of B_0, indicating the rate at which B_0 changes with pressure. This approach provides a reliable framework for use in assessing the structural and mechanical stabilities of these vanadates. The fitted curves reveal smooth energy−volume behaviors, indicating the stabilities and reliabilities of the computational results. Table 2 summarizes the equation of state (EOS) parameters, including the cell volume per formula unit (V_0/Z), B_0, and B_1, of the three calcium vanadates. The calculated B_0 values of CaV_2O_6, $Ca_2V_2O_7$, and $Ca_3V_2O_8$ are 49.79, 75.26, and 72.00 GPa, respectively. Notably, the B_0 of $Ca_3V_2O_8$ aligns closely with the experimental values reported in previous studies [52], indicating the levels of robustness and accuracy of the computational methods used in this study. Moreover, the B_1 values shown in Table 2 in-

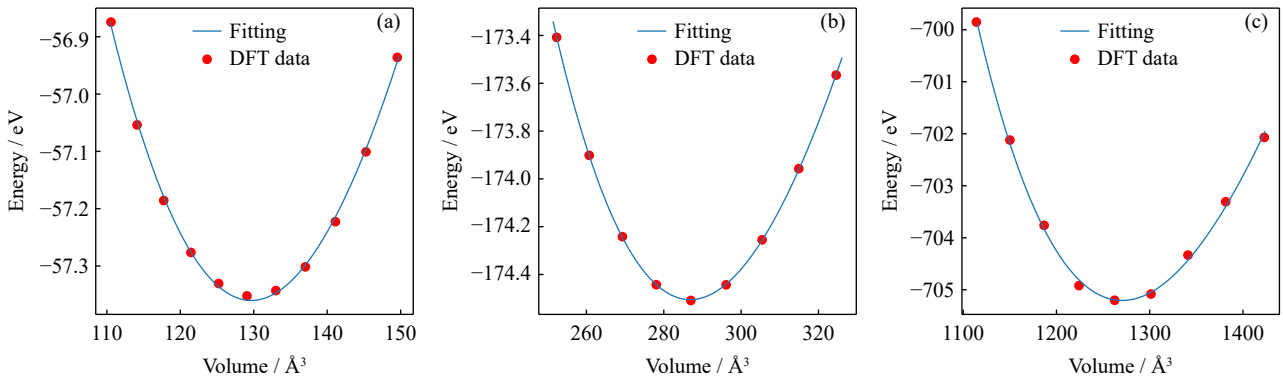

Fig. 2. Energy–volume curves of (a) CaV_2O_6, (b) $Ca_2V_2O_7$, and (c) $Ca_3V_2O_8$, as obtained via DFT calculations and fitted using the Birch equation [51].

crease in the sequence $CaV_2O_6 < Ca_2V_2O_7 < Ca_3V_2O_8$, indicating a progressive enhancement in compressibility from CaV_2O_6 to $Ca_3V_2O_8$. By contrast, the B_0 of 99.08 (2.25) GPa reported by Grzechnik and McMillan [53] was overestimated, likely due to nonhydrostatic stresses during their experiments. Similarly, the B_0 of CaV_2O_6 (49.79 GPa) is highly consistent with that of BaV_2O_6 (50.4 GPa) reported in previous studies [54]. The close agreement between these values may be attributed to the structural similarities between the two compounds, particularly with respect to the CaO_6 octahedral frameworks, which significantly influence their mechanical properties. The differences in the B_0 values of the three compounds reflect variations in their structural rigidities and bonding characteristics, which are influenced by the distinct coordination environments of vanadium and calcium within their crystal structures. These findings provide valuable insights into the mechanical properties of calcium vanadates and a solid foundation for use in the future exploration of their potential applications in the mechanical and optoelectronic fields.

Table 2. EOS parameters, including cell volume per formula unit (V_0/Z), bulk modulus (B_0), and pressure derivative (B_1), of monoclinic CaV_2O_6, $Ca_2V_2O_7$, and $Ca_3V_2O_8$ obtained in this study compared to values reported in previous studies [52]

Structure	Method	(V_0/Z) / Å^3	B_0 / GPa	B_1
CaV_2O_6	DFT (this work)	130.40	49.79	1.28
$Ca_2V_2O_7$	DFT (this work)	300.78	75.26	3.15
$Ca_3V_2O_8$	DFT (this work)	186.67	72.00	4.92
	DFT (Ref. [52])	181.53	68.20	4 (fixed)
	Experiment (Ref. [52])	182.83	69.00	3.7

Fig. 3(a) shows the UV–vis absorption spectra of the samples, and the CaV_2O_6, $Ca_2V_2O_7$, and $Ca_3V_2O_8$ powders exhibit strong degrees of band-to-band absorption in the ranges 200–580, 200–500, and 200–480 nm, respectively. The extended absorption tails observed at approximately 580, 500, and 480 nm in the spectra are attributed to crystal defects formed during multiple high-temperature calcination processes. Although the Tauc equation may slightly underestimate band gaps, it remains one of the most widely used and reliable methods of evaluating optical band gaps [55]. According to the Tauc equation (Fig. 3(b)), the calculated optical band gap of CaV_2O_6 is 2.55 eV, which is consistent with the previously reported values of 2.65 [56] and 2.62 eV [31]. Similarly, the optical band gap of $Ca_2V_2O_7$ is 2.61 eV, aligning well with the reported values of 2.7 [29] and 2.67 eV [57]. The optical band gap of $Ca_3V_2O_8$ is 3.36 eV, which is consistent with the previously reported value of 3.55 eV [58]. These results confirm the high purities of the synthesized samples and reliabilities of the experimental measurements. The equation is expressed as $(\alpha h\nu)^{1/2} = A(h\nu - E_g)$, where α, ν, A, h, and E_g respectively represent the absorption coefficient, light frequency, proportionality constant, planck constant, and optical band gap. First-principles calculations are widely used in calculating various properties of solid-state materials. However, certain systems require extensions and corrections beyond conventional DFT because standard functionals, such as PBE or PBEsol, underestimate the band gaps [59–60]. For example, in strongly correlated systems with localized electrons (such as 3d and 4f electrons), the DFT + U method is often employed. This approach introduces an *on-site* Coulomb repulsion term from the Hubbard model into DFT [61–63], incorporating local Coulomb interaction (U) and exchange (J) parameters to account for Coulomb and exchange interactions within localized d or f orbitals. However, the DFT + U method is ineffective for calcium vanadates. As shown in Fig. 3(c), comparing the band gaps calculated using DFT and DFT + U reveals that, similar to most materials, increasing U results in an overestimation of the band gap. Notably, when $U = 0$, the calculated band gaps are highly consistent with the experimental values, and thus, the standard DFT approach is sufficient to accurately describe the electronic band structures of calcium vanadates, without requiring DFT + U corrections.

To address the lack of research regarding the electronic

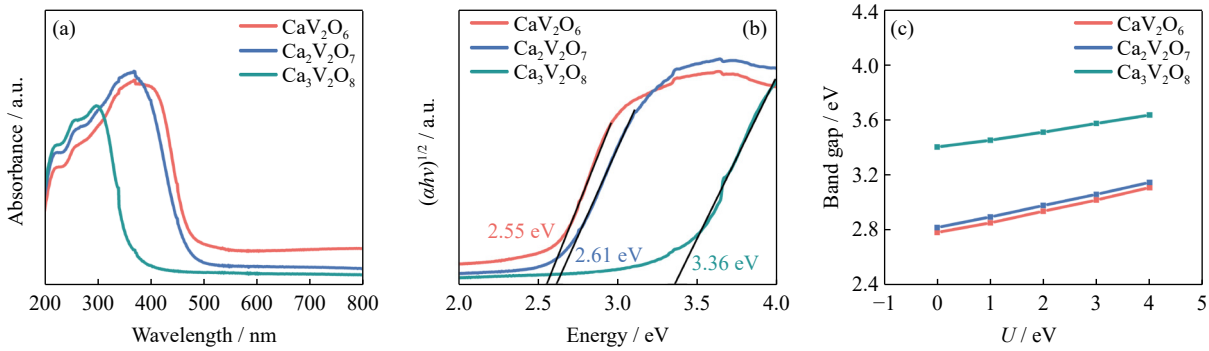

Fig. 3. (a) Transformed UV–vis absorption spectra and (b) calculated band gaps of CaV_2O_6, $Ca_2V_2O_7$, and $Ca_3V_2O_8$, as determined using the Tauc equation. (c) Band gaps of CaV_2O_6, $Ca_2V_2O_7$, and $Ca_3V_2O_8$, as calculated using different *U* values.

properties of CaV_2O_6, $Ca_2V_2O_7$, and $Ca_3V_2O_8$, we analyzed their band structures, as shown in Fig. 4(a)–(d). CaV_2O_6 is an indirect band gap semiconductor, with a band gap of 2.78 eV, where the valence band maximum (VBM) and conduction band minimum (CBM) are observed at the high-symmetry points Y and V, respectively. The valence bands close to the Fermi level are predominantly contributed by O atoms, whereas the V atoms primarily influence the conduction bands. The density of states indicates that the conduction bands are localized, reflecting the contributions of the V 3d orbitals. Similarly, $Ca_2V_2O_7$ exhibits an indirect band gap of 2.81 eV, with the VBM and CBM observed at the T and X points in momentum space. Notably, the conduction bands of $Ca_2V_2O_7$ are flattened, suggesting a heavier effective mass than that of CaV_2O_6. $Ca_3V_2O_8$ is an indirect band gap semiconductor with a larger band gap (3.46 eV), and the VBM and CBM are not observed at the high-symmetry points of the Brillouin zone. The valence and conduction bands are further flattened, indicating increased orbital localization. The narrowband spreading of the density of states further supports our hypothesis. The slopes of the VBM and CBM of CaV_2O_6 are significantly higher than those of $Ca_2V_2O_7$ and $Ca_3V_2O_8$, indicating a smaller effective mass and potentially higher charge carrier mobility. Therefore, of these three materials, CaV_2O_6 is advantageous for application in electronic devices. Remarkably, the calculated band gaps are larger than the experimental values, contrary to the typical underestimation observed with the PBE functional, let alone the PBE + *U*

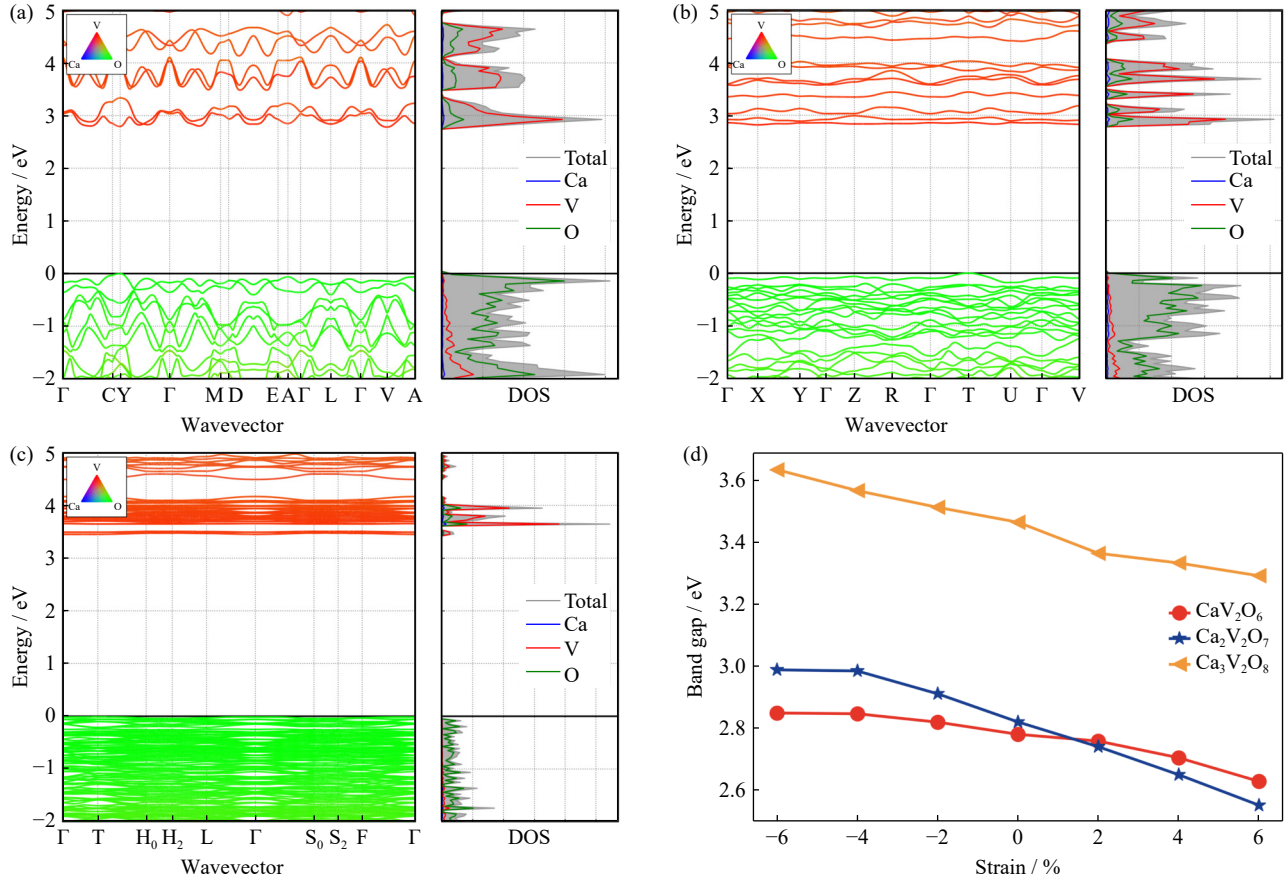

Fig. 4. Electronic band structures and the corresponding electronic densities of states (DOSs) of (a) CaV_2O_6, (b) $Ca_2V_2O_7$, and (c) $Ca_3V_2O_8$. (d) Dependences of the band gaps of the three calcium vanadates on the applied tensile and compressive strains.

methods. These findings suggest that the conventional PBE + *U* methods may be unsuitable for calcium metavanadate because of calculation errors in the lattice constants. To accurately determine the band gap, we applied a slight structural strain of −6% to 6% (Fig. 4(d)). At specific stress levels, the band gaps of the three calcium vanadates decrease with increasing strain, indicating the potential of strain engineering as a method of modulating the band gaps, thus affecting the optoelectronic properties. These reductions in the band gaps are consistent with the behaviors of vanadates under external pressures [64]. Our band structure calculations reveal that the VBM is dominated by O 2p orbitals, whereas the CBM consists of contributions from the V 3d and O 2p orbitals. The enhanced strain-induced hybridization between the V 3d and O 2p orbitals drives the narrowing of the observed band gap, highlighting the versatility of strain engineering in tuning electronic properties. The significant deviation of the band gap of $Ca_3V_2O_8$ from the experimental value is primarily attributed to the mismatch of the exchange-correlation functional. Nevertheless, the observed trend in band gap evolution with applied strain offers valuable insights that can be leveraged in future investigations.

DFT is a powerful, reliable tool for use in accurately predicting and analyzing the optical properties of materials. In this study, we investigated the linear optical properties of CaV_2O_6, $Ca_2V_2O_7$, and $Ca_3V_2O_8$ to provide insights into their potential for application in optoelectronic devices. $Ca_3V_2O_8$ was not considered in these optical calculations owing to its large band gap. The linear optical properties of a semiconductor can be derived from the frequency-dependent real ($\varepsilon_1(\omega)$) and imaginary ($\varepsilon_2(\omega)$) components of the dielectric function $\varepsilon(\omega)$, i.e., $\varepsilon(\omega) = \varepsilon_1(\omega) + \varepsilon_2(\omega)$. The frequency-dependent linear optical properties, including the absorption coefficient $\alpha(\omega)$, energy loss function $L(\omega)$, refractive index $n(\omega)$, and reflectivity $R(\omega)$, can be computed using $\varepsilon_1(\omega)$ and $\varepsilon_2(\omega)$ [65], as shown in Fig. 5(a)–(d). At wavelengths shorter than ~270 nm, the calculated α (Fig. 5(a)) deviates from the experimental data, which is mainly caused by the use of the independent particle approximation (IPA), including local field effects beyond the random phase approximation. More accurate results can be obtained using the Bethe–Salpeter equation (BSE), in addition to the G_0W_0 approximation (G_0W_0-BSE), which is not considered here because of computational limitations. At wavelengths of 300–380 nm, the absorption spectrum of $Ca_2V_2O_7$ is superior to that of CaV_2O_6, exhibiting good consistency with the experimental data. At wavelengths of 380–400 nm, CaV_2O_6 and $Ca_2V_2O_7$ still exhibit absorption capacities, suggesting enhanced levels of purple light absorption. The refractive index and reflectivity of CaV_2O_6 are superior to those of $Ca_2V_2O_7$ in a larger wavelength range, except for those at wavelengths of 350–400 nm. The extinction coefficients ($k(\omega)$) shown in Fig. 5(d) show similar trends to the coefficients shown in Fig. 5(a), revealing the stronger absorption capacity of CaV_2O_6 for purple light.

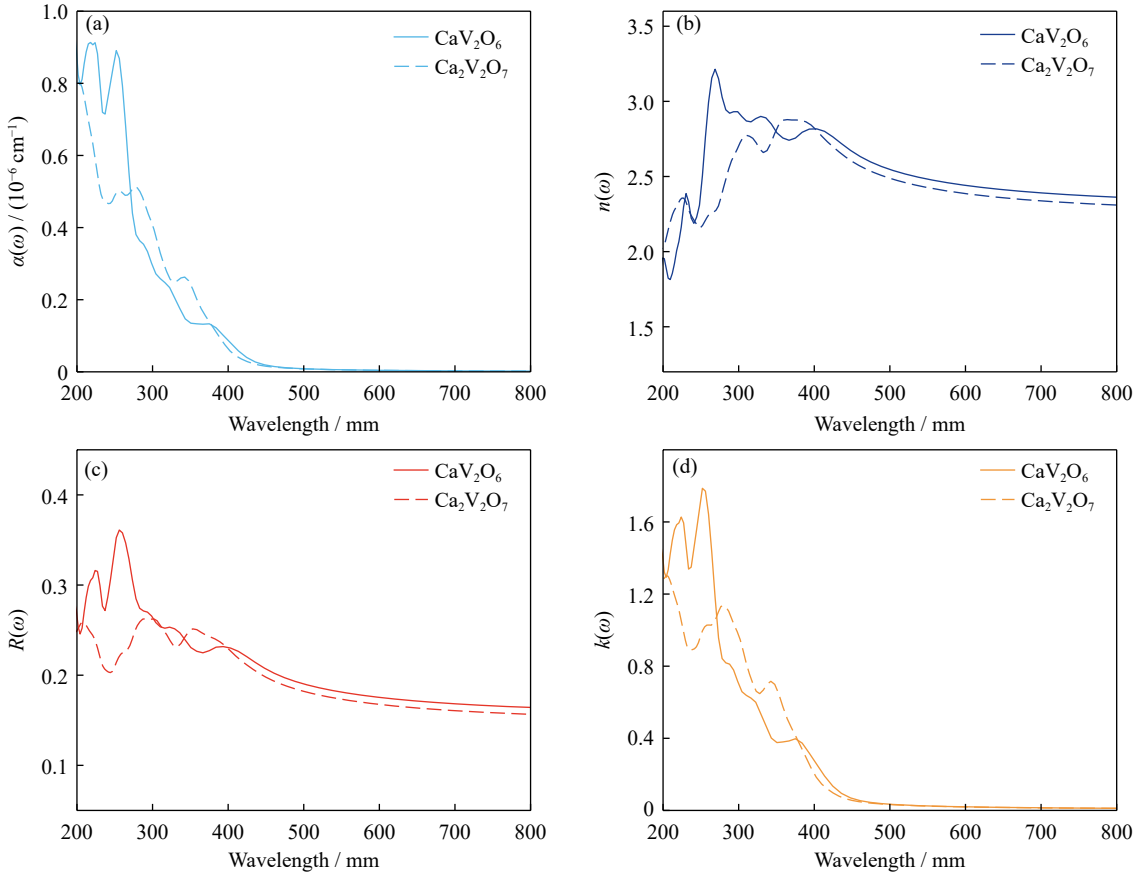

Fig. 5. Optical properties calculated using the IPA, which includes local field effects: (a) absorption coefficients, (b) refractive indices, (c) reflectivities, and (d) extinction coefficients of CaV_2O_6 and $Ca_2V_2O_7$.

PL and CL measurements were performed to evaluate the luminescence properties of CaV_2O_6, $Ca_2V_2O_7$, and $Ca_3V_2O_8$. Fig. 6(a) shows the normalized PL spectra of the three vanadates, which show intense wide emission bands spanning nearly the full spectrum of visible light. The maximum emission peaks of CaV_2O_6, $Ca_2V_2O_7$, and $Ca_3V_2O_8$ are observed at 620, 540, and 510 nm, respectively. Analyzing the PL spectra indicates that these emission peaks do not originate from the band edges or transitions. This is based on the following: the band gaps calculated using the optical absorption spectra are 2.55, 2.61, and 3.41 eV, which exceed those of 2.00, 2.29, and 2.43 eV for CaV_2O_6, $Ca_2V_2O_7$, and $Ca_3V_2O_8$, respectively, as derived from the PL spectra. The redshifts of the PL emission peaks, when compared to the UV–vis absorption spectra and band gaps calculated via DFT, may be attributed to defect states, such as oxygen vacancies or donor–acceptor pairs within the polycrystalline samples [50]. As shown in Fig. 6(b), the CL spectra display narrow emission bands, with the emission peaks of CaV_2O_6, $Ca_2V_2O_7$, and $Ca_3V_2O_8$ observed at 590, 640, and 360 nm, respectively. The absorption and emission edges of the samples fall within the visible and near-UV regions, indicating the potential of CaV_2O_6, $Ca_2V_2O_7$, and $Ca_3V_2O_8$ for use as photoactive materials in photocatalysis, lighting, and display applications. Remarkably, Fig. 6(c) shows the variation in the PL emission intensity of CaV_2O_6 under different pressures, as measured using a diamond anvil cell. The data reveal a substantial enhancement in emission intensity with increasing pressure, where even a modest pressure of 0.19 GPa results in a six-fold increase, and the intensity increases nearly 10-fold at 0.88 GPa. These findings underscore the strong sensitivity of CaV_2O_6 to external pressure, suggesting its potential for use in developing pressure-tunable luminescent applications and high-performance optoelectronic devices. Further exploration of the underlying mechanisms may unlock novel opportunities for functional material design.

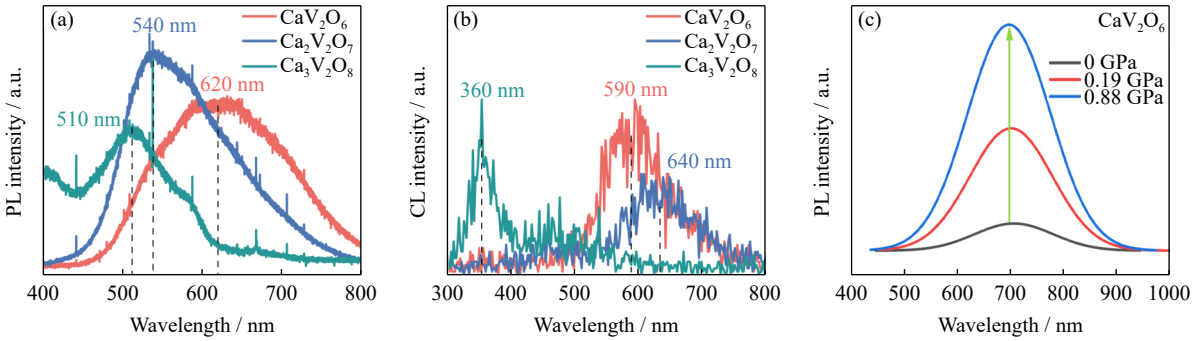

Fig. 6. (a) PL and (b) CL spectra of the prepared CaV_2O_6, $Ca_2V_2O_7$, and $Ca_3V_2O_8$. (c) Changes in the PL emission intensity of CaV_2O_6 under high pressures.

4. Conclusion

In summary, this study presented a detailed investigation of the structures, electronic properties, and luminescence characteristics of three calcium vanadates: CaV_2O_6, $Ca_2V_2O_7$, and $Ca_3V_2O_8$. Based on first-principles calculations, the PBEsol method yielded more accurate lattice parameters compared to the PBE method. Additionally, the PBEsol method could describe the band structures without requiring U correction, thus establishing a reliable foundation for use in subsequent electronic structure analyses. Furthermore, these compounds exhibited significant PL and electroluminescence properties, with CaV_2O_6 and $Ca_2V_2O_7$ emitting red light and $Ca_3V_2O_8$ emitting green light, indicating their potential for application in phosphor materials and optoelectronic devices. The observed redshifts in the luminescence peaks suggested the influences of defect states, further underscoring the complexities of their electronic behaviors. High-pressure experiments further revealed a significant enhancement in the luminescence performance, highlighting the potential for tailoring the optical properties of these materials under various conditions. Overall, this study enhances our understanding of calcium vanadates and paves the way for their future development using advanced material technologies.

Acknowledgements

This work was supported by the National Natural Science Foundation of China (Nos. 12404045 and 52371148), the National Key R&D Program of China (No. 2018YFC1900500), the Foundation of Chongqing Normal University, China (No. 23XLB015), and the Science and Technology Research Program of Chongqing Municipal Education Commission, China (No. KJQN-202400553). Simulations have been performed at the Hefei Advanced Computing Center.

Conflict of Interest

Xuewei Lü is an editorial board member for this journal and was not involved in the editorial review or the decision to publish this article. The authors declare no competing financial interest.

References

[1] M.J. Lee, J. Han, K. Lee, *et al.*, Elastomeric electrolytes for high-energy solid-state lithium batteries, *Nature*, 601(2022), No. 7892, p. 217.

[2] A. VahidMohammadi, J. Rosen, and Y. Gogotsi, The world of two-dimensional carbides and nitrides (MXenes), *Science*,

372(2021), No. 6547, art. No. eabf1581.
[3] T. Yang, D.Z. Jia, B. Xu, *et al*., Textured $CsPbI_3$ nanorods composite fibers for stable high output piezoelectric energy harvester, *eScience*, 4(2024), No. 5, art. No. 100273.
[4] L.L. Zhou, T. Yang, Z. Fang, *et al*., Boosting of water splitting using the chemical energy simultaneously harvested from light, kinetic energy and electrical energy using N doped 4H-SiC nanohole arrays, *Nano Energy*, 104(2022), art. No. 107876.
[5] X. Jin, D.S. Ma, P. Yu, *et al*., Strain-driven phonon topological phase transition impedes thermal transport in titanium monoxide, *Cell Rep. Phys. Sci.*, 5(2024), No. 4, art. No. 101895.
[6] D. Errandonea, S.G. MacLeod, L. Burakovsky, *et al*., Melting curve and phase diagram of vanadium under high-pressure and high-temperature conditions, *Phys. Rev. B*, 100(2019), No. 9, art. No. 094111.
[7] M.G. Stevenson, E.J. Pace, C.V. Storm, *et al*., Pressure-induced bcc-rhombohedral phase transition in vanadium metal, *Phys. Rev. B*, 103(2021), No. 13, art. No. 134103.
[8] X. Jin, Q.L. Ou, H.R. Wei, *et al*., Anomalous thermal transport and high thermoelectric performance of Cu-based vanadate $CuVO_3$, *Appl. Phys. Lett.*, 124(2024), No. 17, art. No. 172203.
[9] J.X. Yang, X.D. Wang, Y.R. Cai, and X.Y. Yang, Corrosion resistance and electrical conductivity of V/Ce conversion coating on magnesium alloy AZ31B, *Int. J. Miner. Metall. Mater.*, 30(2023), No. 4, p. 653.
[10] G. Huyer, S. Liu, J. Kelly, *et al*., Mechanism of inhibition of protein-tyrosine phosphatases by vanadate and pervanadate, *J. Biol. Chem.*, 272(1997), No. 2, p. 843.
[11] X. Jin, M.L. Yuan, H.R. Wei, *et al*., Lattice dynamic and anomalous thermal transport of calcium sodium vanadates, *Int. J. Heat Mass Transf.*, 231(2024), art. No. 125884.
[12] Y. Park, K.J. McDonald, and K.S. Choi, Progress in bismuth vanadate photoanodes for use in solar water oxidation, *Chem. Soc. Rev.*, 42(2013), No. 6, p. 2321.
[13] J. Wen, H.Y. Sun, T. Jiang, B.J. Chen, F.F. Li, and M.X. Liu, Comparison of the interface reaction behaviors of $CaO{-}V_2O_5$ and $MnO_2{-}V_2O_5$ solid-state systems based on the diffusion couple method, *Int. J. Miner. Metall. Mater.*, 30(2023), No. 5, p. 834.
[14] D.W. Xia, H.P. Gao, M.Q. Li, F. Gong, and M. Li, Transition metal vanadates electrodes in lithium-ion batteries: A holistic review, *Energy Storage Mater.*, 35(2021), p. 169.
[15] F. Wan, L.L. Zhang, X. Dai, X.Y. Wang, Z.Q. Niu, and J. Chen, Aqueous rechargeable zinc/sodium vanadate batteries with enhanced performance from simultaneous insertion of dual carriers, *Nat. Commun.*, 9(2018), No. 1, art. No. 1656.
[16] S. Hartung, N. Bucher, J.B. Franklin, *et al*., Mechanism of Na^+ insertion in alkali vanadates and its influence on battery performance, *Adv. Energy Mater.*, 6(2016), No. 9, art. No. 1502336.
[17] X. Jin, X.Y. Ding, F.Y. Zhan, *et al*., Bonding heterogeneity leads to hierarchical and ultralow lattice thermal conductivity in sodium metavanadate, *J. Phys. Chem. Lett.*, 13(2022), No. 48, p. 11160.
[18] Y. Liu, B. Ma, Y. Lü, C. Wang, and Y. Chen, A review of lithium extraction from natural resources, *Int. J. Miner. Metall. Mater.*, 30(2023), No. 2, p. 209.
[19] K. Routray, W. Zhou, C.J. Kiely, and I.E. Wachs, Catalysis science of methanol oxidation over iron vanadate catalysts: Nature of the catalytic active sites, *ACS Catal.*, 1(2011), No. 1, p. 54.
[20] H. Xu, H.M. Li, G.S. Sun, *et al*., Photocatalytic activity of La_2O_3-modified silver vanadates catalyst for Rhodamine B dye degradation under visible light irradiation, *Chem. Eng. J.*, 160(2010), No. 1, p. 33.
[21] F. Chen, Q. Yang, Y.L. Wang, *et al*., Efficient construction of bismuth vanadate-based Z-scheme photocatalyst for simultaneous Cr(VI) reduction and ciprofloxacin oxidation under visible light: Kinetics, degradation pathways and mechanism, *Chem. Eng. J.*, 348(2018), p. 157.
[22] H.M. Fan, D.J. Wang, L.L. Wang, *et al*., Hydrothermal synthesis and photoelectric properties of $BiVO_4$ with different morphologies: An efficient visible-light photocatalyst, *Appl. Surf. Sci.*, 257(2011), No. 17, p. 7758.
[23] T. Kokulnathan, G. Almutairi, S.M. Chen, *et al*., Construction of lanthanum vanadate/functionalized boron nitride nanocomposite: The electrochemical sensor for monitoring of furazolidone, *ACS Sustainable Chem. Eng.*, 9(2021), No. 7, p. 2784.
[24] R. Monsef and M. Salavati-Niasari, Electrochemical sensor based on a chitosan-molybdenum vanadate nanocomposite for detection of hydroxychloroquine in biological samples, *J. Colloid Interface Sci.*, 613(2022), p. 1.
[25] A. Ghosh, Temperature-dependent thermoelectric power of semiconducting bismuth−vanadate glass, *J. Appl. Phys.*, 65(1989), No. 1, p. 227.
[26] D. Souri, Seebeck coefficient of tellurite–vanadate glasses containing molybdenum, *J. Phys. D*, 41(2008), No. 10, art. No. 105102.
[27] J.Y. Xiang, X. Wang, G.S. Pei, Q.Y. Huang, and X.W. Lü, Solid-state reaction of a $CaO{-}V_2O_5$ mixture: A fundamental study for the vanadium extraction process, *Int. J. Miner. Metall. Mater.*, 28(2021), No. 9, p. 1462.
[28] J.C. Bouloux and J. Galy, Structure cristalline de l'hypovanadate CaV_4O_9, *Acta Crystallogr. Sect. B*, 29(1973), No. 6, p. 1335.
[29] X. Jin, G.S. Pei, M.J. Jiao, *et al*., Bonding inhomogeneity and strong anharmonicity induce ultralow lattice thermal conductivity in calcium pyrovanadate, *J. Phys. Chem. C*, 126(2022), No. 38, p. 16492.
[30] P.H. Liang, K.J. Zhu, Y. Rao, *et al*., Hydrated calcium vanadate nanoribbons with a stable structure and fast ion diffusion as a cathode for quasi-solid-state zinc-ion batteries, *ACS Appl. Mater. Interfaces*, 16(2024), No. 19, p. 24723.
[31] X. Jin, X.Y. Ding, Z. Qin, *et al*., Comprehensive study of electronic, optical, and thermophysical properties of metavanadates CaV_2O_6 and MgV_2O_6, *Inorg. Chem.*, 61(2022), No. 44, p. 17623.
[32] W.J. Zhou, M.F. Chen, A.R. Wang, *et al*., Optimizing the electrolyte salt of aqueous zinc-ion batteries based on a high-performance calcium vanadate hydrate cathode material, *J. Energy Chem.*, 52(2021), p. 377.
[33] S.Y. Zhang, K. Wang, Z.H. Hou, *et al*., Calcium vanadate micro/nanostructures for lithium-ion batteries, *ACS Appl. Nano Mater.*, 5(2022), No. 9, p. 12826.
[34] Y.D. Tang, H.Y. Zhang, S.S. Zhang, *et al*., High performance anode for sodium-ion batteries: Calcium pre-intercalated layered vanadium oxide/carbon composite, *Chem. Eng. J.*, 424(2021), art. No. 130378.
[35] H. Kaur and M. Jayasimhadri, Spectroscopic and color tunable studies in Dy^{3+}/Eu^{3+}co-doped calcium–bismuth–vanadate phosphor for lighting applications, *Solid State Sci.*, 122(2021), art. No. 106776.
[36] S.Y. Zhang and W. Mu, Fabrication of $Ca_2V_2O_7$ microspheres and its application in lithium-ion batteries, *Mater. Lett.*, 183(2016), p. 311.
[37] K. Thiagarajan, J. Theerthagiri, R.A. Senthil, and J. Madhavan, Simple and low cost electrode material based on $Ca_2V_2O_7$/PANI nanoplatelets for supercapacitor applications, *J. Mater. Sci.*, 28(2017), p. 17354.
[38] R.J. Yu, N. Xue, S.D. Huo, J.B. Li, and J.Y. Wang, Structure

characteristics and photoactivity of simultaneous luminescence and photocatalysis in CaV_2O_6 nanorods synthesized by the sol–gel Pechini method, *RSC Adv.*, 5(2015), No. 78, p. 63502.
[39] P. Kaur and A. Khanna, Structural, electrical and luminescence properties of $M_2V_2O_7$ (M = Mg, Ca, Sr, Ba, Zn), *J. Mater. Sci.*, 32(2021), p. 21813.
[40] S.S. Parab and A.V. Salker, Structural and optical properties of Tb and Na–Tb co-doped $Ca_3V_2O_8$ phosphors prepared by sol–gel process, *Mater. Res. Express*, 5(2018), No. 1, art. No. 016302.
[41] G. Kresse and J. Hafner, *Ab initio* molecular dynamics for open-shell transition metals, *Phys. Rev. B*, 48(1993), No. 17, p. 13115.
[42] G. Kresse and J. Furthmüller, Efficient iterative schemes for *ab initio* total-energy calculations using a plane-wave basis set, *Phys. Rev. B*, 54(1996), No. 16, p. 11169.
[43] J.P. Perdew, A. Ruzsinszky, G.I. Csonka, *et al.*, Restoring the density-gradient expansion for exchange in solids and surfaces, *Phys. Rev. Lett.*, 100(2008), No. 13, art. No. 136406.
[44] D. Le, A. Kara, E. Schröder, P. Hyldgaard, and T.S. Rahman, Physisorption of nucleobases on graphene: A comparative van der waals study, *J. Phys. Condens. Matter*, 24(2012), No. 42, art. No. 424210.
[45] H.J. Monkhorst and J.D. Pack, Special points for Brillouin-zone integrations, *Phys. Rev. B*, 13(1976), No. 12, p. 5188.
[46] J.C. Bouloux, G. Perez, and J. Galy, Structure cristalline des métavanadates CaV_2O_6 et $CdV_2O_6\alpha$. La transformation polymorphique $CdV_2O_6\alpha \rightleftarrows CdV_2O_6\beta$, *Bull. Soc. fr. Minéral. Cristallogr.*, 95(1972), No. 1, p. 130.
[47] V.K. Trunov, Y.A. Velikodnyi, E.V. Murashova, and V.D. Zhuravlev, Crystal structure of calcium pyrovanadate, *Sov. Phys. Dokl.*, 28(1983), art. No. 425.
[48] R. Gopal and C. Calvo, The structure of $Ca_3(VO_4)_2$, *Z. Für Kristallogr. Cryst. Mater.*, 137(1973), No. 1-6, p. 67.
[49] D.P. Dutta, M. Ramakrishnan, M. Roy, and A. Kumar, Effect of transition metal doping on the photocatalytic properties of $FeVO_4$ nanoparticles, *J. Photochem. Photobiol. A*, 335(2017), p. 102.
[50] X. Jin, R. Wang, Y.Y. Zhou, *et al.*, A comprehensive experimental and first-principles study on magnesium–vanadium oxides, *J. Alloy. Compd.*, 896(2022), art. No. 162862.
[51] K. Latimer, S. Dwaraknath, K. Mathew, D. Winston, and K.A. Persson, Evaluation of thermodynamic equations of state across chemistry and structure in the materials project, *NPJ Comput. Mater.*, 4(2018), art. No. 40.
[52] J. Sánchez-Martín, D. Errandonea, H.S.R. Mosafer, *et al.*, The pressure and temperature evolution of the $Ca_3V_2O_8$ crystal structure using powder X-ray diffraction, *CrystEngComm*, 25(2023), No. 8, p. 1240.
[53] A. Grzechnik and P.F. McMillan, High-pressure X-ray diffraction of $Sr_3(VO_4)_2$ and $Ba_3(VO_4)_2$, *Physica B*, 252(1998), No. 4, p. 268.
[54] P.J. Zhang, P. Botella, N. Bura, *et al.*, High-pressure phase transition and amorphization of BaV_2O_6, *Dalton Trans.*, 54(2025), No. 5, p. 2011.
[55] A.B. Garg, D. Vie, P. Rodriguez-Hernandez, A. Muñoz, A. Segura, and D. Errandonea, Accurate determination of the bandgap energy of the rare-earth niobate series, *J. Phys. Chem. Lett.*, 14(2023), No. 7, p. 1762.
[56] M.S. Islam, H. Kabir, Y. Inagaki, and A.R. Sarker, Comparative study of the conductivity of synthesized bivalent vanadates CaV_2O_6 and MnV_2O_6, *J. Alloy. Compd.*, 829(2020), art. No. 154499.
[57] A. Sharma, M. Varshney, K.H. Chae, and S.O. Won, Electronic structure and luminescence assets in white-light emitting $Ca_2V_2O_7$, $Sr_2V_2O_7$ and $Ba_2V_2O_7$ pyro-vanadates: X-ray absorption spectroscopy investigations, *RSC Adv.*, 8(2018), No. 46, p. 26423.
[58] P. Parhi, V. Manivannan, S. Kohli, and P. McCurdy, Synthesis and characterization of $M_3V_2O_8$ (M = Ca, Sr and Ba) by a solid-state metathesis approach, *Bull. Mater. Sci.*, 31(2008), No. 6, p. 885.
[59] T. Ouahrani, R.M. Boufatah, M. Benaissa, Á. Morales-García, M. Badawi, and D. Errandonea, Effect of intrinsic point defects on the catalytic and electronic properties of Cu_2WS_4 single layer: *Ab initio* calculations, *Phys. Rev. Mater.*, 7(2023), No. 2, art. No. 025403.
[60] Y. Xue, T. Yang, E.H. Wang, *et al.*, Unveiling the contribution of piezoelectric and ferroelectric effect to inorganic halide perovskites photodetectors, *Nano Energy*, 125(2024), art. No. 109491.
[61] D.J. Carrascal, J. Ferrer, J.C. Smith, and K. Burke, The Hubbard dimer: A density functional case study of a many-body problem, *J. Phys. Condens. Matter*, 27(2015), No. 39, art. No. 393001.
[62] H.T. Dang, J. Mravlje, A. Georges, and A.J. Millis, Electronic correlations, magnetism, and Hund's rule coupling in the ruthenium perovskites $SrRuO_3$ and $CaRuO_3$, *Phys. Rev. B*, 91(2015), No. 19, art. No. 195149.
[63] N.X. Yang, M.L. Yuan, J.L. Yang, *et al.*, *Ab initio* investigation of the thermophysical properties of barium orthovanadate, *J. Am. Ceram. Soc.*, 108(2025), No. 4, art. No. e20322.
[64] D. Errandonea and A.B. Garg, Recent progress on the characterization of the high-pressure behaviour of AVO4 orthovanadates, *Prog. Mater. Sci.*, 97(2018), p. 123.
[65] V. Wang, N. Xu, J.C. Liu, G. Tang, and W.T. Geng, VASPKIT: A user-friendly interface facilitating high-throughput computing and analysis using VASP code, *Comput. Phys. Commun.*, 267(2021), art. No. 108033.

2023 Innovative Young Scientist

Xuewei Lü is a professor and Ph.D. advisor at Chongqing University, specializing in iron and steel metallurgy. His research centers on the efficient smelting of complex and refractory ores, with a particular focus on the high-temperature physicochemical properties, structural evolution, and regulation mechanisms of multi-component slag systems. He proposed a technical framework of "slag property regulation to promote efficient smelting", contributing to the development and industrial application of several novel metallurgical technologies. He has led projects supported by the National Natural Science Foundation of China, the National Key R&D Program, and top enterprises such as Baowu, Pangang, and HBIS. He has published over 160 SCI papers, including 77 in the past five years, with over 3000 citations on Web of Science and an H-index of 33. He has authored both Chinese and English monographs, holds 44 invention patents—21 of which have been applied or commercialized—and has delivered plenary talks at numerous international conferences. He serves on editorial boards of major international journals and is an active member of several academic and industry committees in the metallurgy field.